Comparison of CFD–DEM heat transfer simulations with infrared/visual measurements

A.V. Patil, E.A.J.F. Peters *, J.A.M. Kuipers

Multiphase Reactors Group, Department of Chemical Engineering & Chemistry, Eindhoven University of Technology, P.O. Box 513, 5600 MB Eindhoven, The Netherlands

HIGHLIGHTS

- Heat transfer in a fluidized bed is studied both by simulations and experiments.
- Combined visual/IR measurements are compared to CFD–DEM simulation results.
- Particle–particle and particle–wall heat transfer is negligible.
- For a good match a significant amount of gas to wall heat transfer is needed.

ARTICLE INFO

ABSTRACT

A new combined infrared/particle image velocimetry/digital image analysis (IR/PIV/DIA) measuring technique for investigating heat transfer in gas–solid fluidized beds has been recently developed. This new technique gives insightful information and quantitative data on particle volume fractions, particle volume fluxes and temperature distributions in fluidized beds for CFD validations. The current paper compares simultaneous thermal and hydrodynamic data of a pseudo 2-D fluidized bed obtained using this new technique with results from CFD–DEM simulations. An extensive series of time-averaged volume fractions, volume fluxes and temperature distributions as well as instantaneous profiles are presented. This detailed comparison between the experimental and simulated profiles shows the capabilities of state-of-the-art CFD–DEM simulations, and pinpoints where simulation (and also measurement) techniques still can be improved.

1. Introduction

Fluidized beds are frequently used in a variety of processes because of their favorable mass and heat transfer characteristics. Fluidized catalytic cracking, fluidized bed coal combustion and polymerization for production of polyethylene (UNIPOL) are some of the well-known processes where heat transfer plays an important role. In such processes formation of hot spots is a phenomenon which can severely effect the overall performance of a reactor. Thus the study of heat transfer in fluidized beds is of high relevance.

Computational fluid dynamics–discrete element method (CFD–DEM) is an Euler–Lagrange method that is suited for modeling fluidized beds at the lab scale. CFD–DEM modeling of dense gas–solid flow is based on continuum fixed-grid (Eulerian) modeling of the gas phase and discrete (Lagrangian) modeling of the particulate

phase. A drag law is used to account for the momentum exchange between the continuum and particulate phase in a two-way coupled manner [1,2]. This CFD–DEM model was extended previously with gas–solid two-way-coupling for heat transfer. Details on this can be found in Patil et al. [3].

In the current paper additional mechanisms of heat exchange are introduced in the CFD–DEM code in order to further improve the description of non-isothermal systems. These new mechanisms are particle–particle direct contact conduction, particle–wall direct contact conduction and gas–wall convective heat transfer. The implementations of particle–particle and particle–wall heat transfer are based on theoretical developments proposed by Sun and Chen [4] and Zhang and Whiten [5]. These theoretical expressions have been used before by others to model heat-transfer in multiphase flow [6–8]. Some of these adaptations have also been used for CFD–DEM implementations, e.g., by Zhou and Zulli [9]. Although the theoretical concepts used are similar, our implementation differs markedly from the one used in that paper. This will be discussed extensively in Section 2.3.

* Corresponding author. Tel.: +31 40 247 3122; fax: +31 40 247 5833.
  E-mail address: e.a.j.f.peters@tue.nl (E.A.J.F. Peters).

A few CFD–DEM simulation studies on heat transfer in gas–solid fluidized beds can be found in literature [10,9,11]. However, this is the first time (as far as the authors are aware) that a direct comparison is presented of CFD–DEM simulation results with detailed infrared/visual measurements. This was not possible until recently due to the limitations on experimental techniques available.

Some of the commonly known techniques used for fluidized bed studies are electrical capacitance tomography, X-ray tomography, magnetic resonance particle tracking or positron emission particle tracking and particle image velocimetry (PIV) which were all limited to hydrodynamic investigations [12–16]. The technique we used extends the PIV/DIA technique of van Buijtenen et al. [17] and de Jong et al. [18] to investigate the hydrodynamics of pseudo-2D fluidized beds, with spatial infrared thermography. Infrared thermography is a mature measurement technique (see Kaplan [19]). However, the combination of thermography with PIV/DIA was introduced only recently in Patil et al. [20]. This technique provides integrated data consisting of spatially resolved mass, velocity and temperature distributions in a pseudo 2-D fluidized bed. Similar data-sets can be obtained from CFD–DEM simulations and used to perform a direct comparison with the experiment.

We will start with describing the CFD–DEM modeling method that has been used for non-isothermal dense gas-particle flows. The various other mechanisms of heat transfer are also described in this Section 2. A brief description on the experimental technique that was used is discussed in Section 3. Detailed information on the technique can be found in Patil et al. [20]. This will be followed by comparisons between experimental and simulation data of the hydrodynamic and thermal data in Section 4 for the case of a cooling pseudo-2D fluidized bed.

2. Modeling method

2.1. Gas phase modeling

The volume-averaged conservation equations for gas phase mass and momentum are given by;

$$\frac{\partial}{\partial t}\left(\varepsilon_f \rho_f\right) + \nabla \cdot \left(\varepsilon_f \rho_f \mathbf{u}\right) = 0, \tag{1}$$

$$\frac{\partial}{\partial t}\left(\varepsilon_f \rho_f \mathbf{u}\right) + \nabla \cdot \left(\varepsilon_f \rho_f \mathbf{uu}\right) = -\varepsilon_f \nabla p - \nabla \cdot \left(\varepsilon_f \boldsymbol{\tau}_f\right) + \mathbf{S}_p + \varepsilon_f \rho_f \mathbf{g}, \tag{2}$$

where $\mathbf{S}_p$ represents the source term for momentum originating from the particulate phase and is given by

$$\mathbf{S}_p = \sum_a \frac{\beta V_a}{1 - \varepsilon_f}(\mathbf{v}_a - \mathbf{u})\delta(\mathbf{r} - \mathbf{r}_a) \equiv \boldsymbol{\alpha} - \beta \mathbf{u}. \tag{3}$$

In our equations we use the convention that the subscript f indicated the fluid phase (i.e., gas in this case) and p the particulate phase. For example, ε_f indicates the fluid volume fraction or porosity. Individual particles are labeled by the subscript a. For the fluid velocity we use $\mathbf{u}$ and for particle velocities $\mathbf{v}$. In the above expression, β represent the gas particle drag coefficient and $\boldsymbol{\alpha}$ represents all momentum creation per unit volume due to the pressure of the moving particles. The drag coefficient, β, is evaluated by the [21] equation for gas-particle drag,

$$\beta = \frac{10(1 - \varepsilon_f)}{\varepsilon_f^2} + \varepsilon_f^2(1 + 1.5(1 - \varepsilon_f)^{0.5})$$

$$+ \frac{0.413 \text{Re}_p}{24 \varepsilon_f^2}\left[\frac{\varepsilon_f^{-1} + 3\varepsilon_f(1 - \varepsilon_f) + 8.4 \text{Re}_p^{-0.343}}{1 + 10^{3(1-\varepsilon_f)} \text{Re}_p^{-\frac{1+4(1-\varepsilon_f)}{2}}}\right], \tag{4}$$

The definition for the particle Reynolds number will be given below.

The thermal energy equation for the fluid is given by,

$$\frac{\partial\left(\epsilon_f \rho_f C_{p,f} T\right)}{\partial t} + \nabla \cdot \left(\epsilon_f \rho_f \mathbf{u} C_{p,f} T\right) = \nabla \cdot \left(\epsilon_f k_f^{\text{eff}} \nabla T\right) + Q_p, \tag{5}$$

where Q_p represents the source term originating from interphase energy transport whereas k_f^{eff} is the effective thermal conductivity of the fluid phase that can be expressed in terms of the microscopic fluid thermal conductivity, k_f, as

$$k_f^{\text{eff}} = \frac{1 - \sqrt{1 - \epsilon_f}}{\epsilon_f} k_f. \tag{6}$$

This equation was originally proposed by Syamlal and Gidaspow [22]. The source term due to the heat transfer of the particles to the fluid can be obtained by summing the contributions of all particles using a (smoothed) delta-function as,

$$Q_p = -\sum_a Q_a \delta(\mathbf{r} - \mathbf{r}_a) = \sum_a h_{fp} A_a (T_a - T_f)\delta(\mathbf{r} - \mathbf{r}_a), \tag{7}$$

where Q_a is the heat transferred from the fluid to particle a. It is expressed by a temperature difference and a heat transfer coefficient h_{fp}. For this parameter we use the empirical correlation given by [23],

$$\text{Nu}_p = (7 - 10\epsilon_f + 5\epsilon_f^2)\left[1 + 0.7\text{Re}_p^{0.2}\text{Pr}^{0.33}\right]$$

$$+ (1.33 - 2.40\epsilon_f + 1.20\epsilon_f^2)\text{Re}_p^{0.7}\text{Pr}^{0.33} \tag{8}$$

where,

$$\text{Nu}_p = \frac{h_{fp} d_p}{k_f}, \quad \text{Re}_p = \frac{d_p \epsilon_f \rho_f |\mathbf{u} - \mathbf{v}|}{\mu_f} \quad \text{and} \quad \text{Pr} = \frac{\mu_f C_{p,f}}{k_f}. \tag{9}$$

The particle Reynolds number is calculated foe each individual particle with the fluid velocity, $\mathbf{u}$, evaluated at the its center of mass position. Note that the fluid density is obtained by means of ideal gas law equation-of-state. Since the system is non-isothermal this means that the density is position dependent. Via the density-dependence of Re_p this will influence the local Nusselt numbers and thus effect the heat-transfer coefficients a little. In our simulations we did not take into account possible temperature dependency of the viscosity as it does not vary much over the small temperature range of our system (i.e., 20–100 °C).

2.2. Discrete particle phase

The particle phase modeling is based on tracking individual particles. The motion of a single spherical particle a with mass m_a and moment of inertia I_a is described by Newton's equations:

$$m_a \frac{d^2 \mathbf{r}_a}{dt^2} = -V_a \nabla p + \frac{\beta V_a}{1 - \varepsilon_f}(\mathbf{u} - \mathbf{v}_a) + m_a \mathbf{g} + F_{\text{contact},a} \tag{10}$$

$$I_a \frac{d\boldsymbol{\omega}_a}{dt} = \boldsymbol{\tau}_a \tag{11}$$

where $\mathbf{r}_a$ is the particle position. The forces on the right-hand side of Eq. (10) are due to the pressure gradient, drag, gravity and contact forces due to collisions, $\boldsymbol{\tau}_a$ is the torque, and $\boldsymbol{\omega}_a$ the angular velocity.

To evaluate the heat transfer from the fluid to the particles the gas temperature is interpolated from the surrounding grid points to the particle center of mass position. This interpolated gas temperature is represented as T_f. The heat balance on particle a gives an evolution-equation for its temperature, T_a,

$$Q_a = \rho_a V_a C_{p,a} \frac{dT_a}{dt} = h_{fp} A_a (T_f - T_a). \tag{12}$$

2.3. Particle–particle and particle–wall heat transfer

When particles collide with each other or with the wall heat is conducted through the contact area. Since collision contacts last for a very short time (10^{-6} s) the amount of heat transferred during a single collision is very small. However, thousands of such collisions take place for each of the individual particles in dense particulate flows. Thus over longer time scales the amount of heat transferred may become significant.

An implementation accounting for this type of heat transfer is now presented, which differs from some of the previous works, such as [9,11,24]. The CFD–DEM implementation of Zhou and Zulli [9] uses the Hertzian model for collision dynamics whereas in our case Cundall and Strack [25] model is used. Let us first emphasize that the collision time and 'contact' area as determined from the soft sphere model has no physical meaning. In the soft sphere model of DEM the simulation spring stiffness is much less than the real spring stiffness of real particles, so that bigger DEM time steps can be taken for simulations, while keeping the overlap within acceptable bounds. The overlap is kept under 0.1% of the particle diameter for a particle relative velocity that is twice the fluidization velocity. Due to the reduced spring stiffness the contact area calculated in a soft-sphere simulation is higher than the contact area prevailing in a 'real' collision leading to an exaggerated heat transfer between particles. Thus in the proposal made by Zhou and Zulli [9], Zhou et al. [11] and Hou et al. [24] a correction factor was used to obtain the corrected contact area and hence a corrected heat transfer rate for each of the DEM time steps. This correction is based on the theoretical calculation of the contact area proposed by Sun and Chen [4] and Zhang and Whiten [5]. This method of discrete energy transfer at each DEM time step is computationally expensive.

In our modeling methodology for particle mechanics we use a simpler method. Instead of a correction we calculate the correct total heat or energy transfer during one collision and directly transfer it as a packet of energy at the beginning of the collision. This calculation is based on the Sun and Chen [4] model where the integral amount of energy transferred during a collision has been theoretically derived. This integral is calculated from the 'real' particle properties, relative velocity, etc. as primary parameters. These primary parameters also give the maximum contact area and contact time which are both required in the expression for the amount of transferred heat given below in Eq. (13).

Note that this approach can easily be implemented in DEM because here a contact list is maintained and the first encounter of two particles is explicitly detected. Furthermore the amount of heat transferred during one particle–collision is so small that it does not give rise to numerical issues if it is transferred instantaneously, instead of smearing it out over the full duration of a collision. The total amount of heat transferred during one collision equals

$$q_c = \frac{0.87(T_1 - T_2)A_c t_c^{1/2}}{(\rho_1 C_{p,1} k_1)^{(-1/2)} + (\rho_2 C_{p,2} k_2)^{(-1/2)}}, \tag{13}$$

where, A_c, is the maximum contact area,

$$A_c = \pi r_c^2 = \pi \left(\frac{5m}{4E}\right)^{\frac{2}{5}} (R v_{\text{rel}})^{4/5}, \tag{14}$$

while the total contact duration equals,

$$t_c = 2.94 \left(\frac{5m}{4E}\right)^{\frac{2}{5}} (R v_{\text{rel}})^{-1/5}, \tag{15}$$

The parameters in the above equations, for 2 particles (1 and 2) involved in a collision, are: $R = R_1 R_2/(R_1 + R_2)$, $m = m_1 m_2/(m_1 + m_2)$ where E is an overall elastic modulus which is a function of Young's moduli (E_1 and E_2) and Poisson's ratios (v_1 and v_2),

$$E = \frac{4}{3} \left(\frac{1 - v_1^2}{E_1} + \frac{1 - v_2^2}{E_2}\right)^{-1}. \tag{16}$$

The same expression can be used for a particle wall collision, when a wall is considered to be a sphere with infinite radius ($R_2 \to \infty$), such that $R = R_1$, and an infinite mass, such that $m = m_1$. In this case, clearly, $T_2 = T_w$ and for the properties of 'particle 2' the properties of the material of the wall need to be used. The wall temperature, T_w, is the bulk wall temperature which is 20 °C in our case. The relevant material properties are tabulated in Table 1.

2.4. Gas–wall heat transfer

The gas–wall heat loss is accounted for in the CFD–DEM by a boundary condition imposed on the gas phase thermal energy equation. Due to the vigorous mixing and tortuous motion of gas in fluidized beds it can be said that most of the temperature gradient and heat transfer resistance lies very close to the wall, see Fig. 1. An alternative way of observing this is that the resistance to heat transfer lies within a thin film layer smaller than the size of a particle. In CFD–DEM the grid size used to solve the gas dynamics is much larger than the width of this film. Therefore the film is unresolved and the heat-transfer from gas to wall should be modeled using a heat transfer coefficient. This heat transfer coefficient is represented by

$$h_w = k_g/\delta_l, \tag{17}$$

where, δ_l is the thickness of the thin film layer across which most of the resistance to heat transfer is concentrated. There might also be some resistance to heat transfer in the wall itself, but this will be a minor contribution compared to the gas layer. The external temperature, or the temperature deep in the wall, is assumed to be the environment temperature that is $T_{\text{ext}} = 20$ °C. A typical boundary condition for the gas temperature (for a wall in the zy-plane) is

$$-k_g^{\text{eff}} \frac{dT_g}{dx} = h_w(T_w - T_g). \tag{18}$$

Boundary cells are shown in Fig. 2 where the temperature, being a scalar quantity, is defined cell centered in a staggered grid system. Discretization of Eq. (18) leads to

$$T_{g,0} = \frac{2k_f^{\text{eff}} - h_w \Delta x}{2k_f^{\text{eff}} + h_w \Delta x} T_{g,1} + \frac{2h_w \Delta x}{2k_f^{\text{eff}} + h_w \Delta x} T_w. \tag{19}$$

It should be noted that this heat transfer coefficient does not accommodate for direct particle–wall collision contact heat transfer. This contribution is accounted for separately in the way discussed in the previous subsection.

The gas–wall heat transfer coefficient term, h_w, is unknown. It should follow from more detailed simulations, like DNS, that resolve the film layer or from correlations. The heat transfer coefficient between the gas and the wall is hard to determine experimentally. Previously, wall to emulsion phase heat-transfer

Table 1
Material properties needed to compute particle–particle and particle–wall heat transfer.

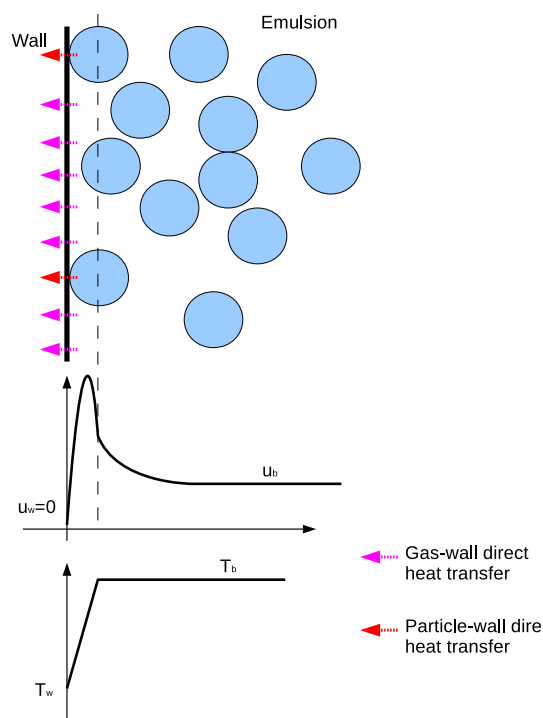| Properties	Glass	Aluminum	Sapphire glass
Poisson ratio (–)	0.22	0.34	0.25
Young's modulus (GPa)	60	69	35
Thermal conductivity (W/m K)	1.4	30	30
Heat capacity (J/kg K)	840	2700	3980

Fig. 1. A schematic view diagram showing the mechanisms by which the fluidized bed looses heat to the surrounding walls.

correlations have been proposed. In [26] the proposed equation by Glicksman, Decker and Baskakov is given,

$$\text{Nu} = \frac{h_w d_p}{k_g} = \begin{cases} 5.0 + 0.05\text{Pr}\text{Re}_p & \text{if } \text{Re}_p < 150 \\ 0.18\text{Pr}^{0.33}\text{Re}_p^{0.8} & \text{if } \text{Re}_p > 150. \end{cases} \quad (20)$$

This correlation gives a value between 200 and 350 W/m² K for our systems. Since gas to wall heat transfer only contributes partly to the full emulsion to wall heat transfer, h_w is expected to be of this magnitude or smaller. In our comparison of simulations with experiments h_w will be used as a fitting parameter to match the two data sets. This fitting of simulations with experiments using wall heat loss coefficient h_w will be discussed in Section 4.

2.5. Other mechanisms of heat transfer

Though most of the known important mechanisms of heat transfer have been included in the model some complex forms of heat transfer that are difficult to model have been left out. One of these forms is radiation. However, for our relative low temperatures this mechanism will only be of minor importance.
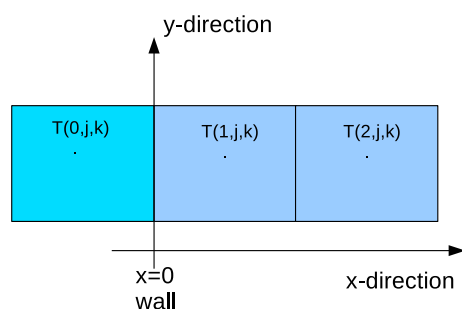

Fig. 2. Eulerian grid and relevant temperatures for the treatment of the boundary condition.

During fluidization particles are constantly colliding with the walls. The heat transfer during collision has been accounted for and described earlier in this section. However, this is not the only form of particle wall interaction that occurs. Clusters of particles are flowing along the wall. These particles roll and brush against the wall. Unlike collision where contact times are low (<10⁻⁵ s) particles brushing against the wall remain at the wall for a much longer time (<10⁻⁵ s). Though the contact time in the later form of contact is higher it cannot be said that this is a stronger mechanism of heat transfer. This is because though collision times are small they take place more frequently in comparison to rolling against the wall.

Another form of unaccounted heat transfer in the model is due to clusters of particles coming to momentary rest near the bottom distributor plate of the bed or against the wall while fluidizing. This momentary stagnation prevails for circulating particles after coming down along a wall. It leads to longer contact time for such a particle in the region near the bottom compared to collisions. Heat transfer of particle assemblies with low mobility are treated in current CFD–DEM as collisions where a very small contact time would be considered and a smaller packet of energy is transferred. However, the contacts are not really collisional but of a more lasting nature.

The modeling of heat transfer in this less mobile dense particle regions near the wall and bottom is difficult. Especially its incorporation into the CFD–DEM, because temperature gradients on the scale of particles are not available. One might consider to add a solids contribution to the effective conductivity k^{eff}, where we now only consider a gas contribution (see Eq. (6)). In CFD–DEM it is a bit unnatural to model the solids phase in an effective way because the particle phase is resolved.

Since we do not currently know how to treat the heat transfer through less mobile regions we neglected this form of heat transfer. Earlier we mentioned that gas–wall heat transfer coefficient h_w will be used as a fitting parameter. So, the heat loss due to non-modeled mechanisms will eventually be lumped into an overall, fitted or modeled gas–wall heat transfer coefficient. From the fact whether the fitting gives reasonable numbers (or is possible at all) we will evaluate the significance of non-modeled mechanisms.

It should be noted that in reality the unknown mechanisms of heat transfer are not necessarily from gas to wall. It was nevertheless modeled as part of the gas–wall heat transfer coefficient, h_w, because it was included in the simulations viaEq. (19). Therefore we will name it the 'fitted' gas–wall heat transfer coefficient.

3. Experimental imaging method and simulation data

3.1. Experimental and simulation setup

A series of fluidization experiments using the visual/infrared imaging technique were performed on a pseudo 2-D fluidized bed setup. The details of the recently developed experimental image analysis can be found in [20]. Here, in this section, we will only briefly discuss the experimental setup and the data analysis of the measurements.

The fluidization runs were carried out with glass particle of size 1 mm which can be classified as Geldart D type particles. The particle properties are provided in Table 2. Hot particles, heated in an oven at 120 °C, were charged into the empty bed at room temperature, after which a constant nitrogen gas stream at 20 °C is supplied through the bottom plate. The used bed consisted of aluminum back and side walls and a front window made of sapphire glass.

The size of the experimental pseudo 2-D bed was (width × height × depth) 8 cm × 25 cm × 1.5 cm. The fluidization gas enters from the bottom perforated support. The setup had a

Table 2
Properties and settings used in the experiments and simulations.

Particle material			Glass
(a) Constant particle and fluid properties			
Particle density ρ_p			2500 kg/m^3
Norm. coeff. of restit.			0.97
Tang. coeff. of restit.			0.33
Fluid heat capacity C_{pf}			1010 J/kg K
Particle heat capacity $C_{p,a}$			840 J/kg K
Fluid viscosity μ_f			2.0×10^{-5} kg/ms
d_p (mm)	Geldart type	u_{bg} (m/s)	Bed mass (g)
(b) Settings used in experiments			
1.0	D	1.20	75 & 125
1.0	D	1.54	75 & 125
1.0	D	1.71	75 & 125

small circular nozzle of size 1.2 cm in size shown in Fig. 3. No gas entered from this nozzle during the experiments. The nozzle as such had no special purpose. It was part of the set up that was developed for injecting hot gas, but in this cooling bed experiment only cold background gas was used and the nozzle inlet gas was switched off.

For the fluidization of the 1 mm particles two bed-heights corresponding to bed masses of 75 g and 125 g were considered and three background gas velocities were used. The properties and settings for the fluidization experiments and simulations are summarized in Table 2. The background velocity given in that table is actually the total volumetric flow rate divided by the cross sectional area of the bed. Note that this does not equal the velocity that is supplied through the porous plate because of the presence of the nozzle where there is no gas flow. The nozzle occupies 10% of the bottom plate area. So, e.g., for u_{bg} = 1.2 m/s in Table 2 the actual superficial velocity through the bottom porous plate equals (1.2/0.9) i.e. 1.33 m/s.

The CFD–DEM simulations were performed for the same setup dimensions, material properties and experimental settings. The gas phase flow was modeled on a Eulerian grid (NX × NY × NZ) of 35 × 110 × 6. So the size of individual block mesh was (DX × DZ × DY) 2.28 mm × 2.28 mm × 2.5 mm. This size was chosen to match the interrogation grid size of the DIA/PIV technique

which was 2.28 times the particle size [20]. Because the bed with its depth of 1.5 cm was pseudo 2-D, the hydrodynamic and thermal variations in the depth direction were negligible. We therefore present 2D data obtained by averaging over the depth direction.

The fact that no gas entered from the nozzle needed to be incorporated in the simulations so that the computed spatial gas distribution is identical to that in the experiments. However, the CFD–DEM simulations were performed with a block mesh Eulerian grid while the real nozzle was circular. To mimic the nozzle a no-flow boundary condition was set for 5 × 4 grid cells which was 1.14 cm × 1 cm in size (i.e. nearly the same area as the nozzle). For the boundary condition at the other bottom cells a velocity corresponding to the corrected background velocity as discussed in the previous paragraph was set.

3.2. Data acquisition and analysis

The fluidizing bed was recorded by both a visual camera (La Vision ImagePro, 560 × 1280 resolution) and an infrared camera (FLIR SC7600, 250 × 512 resolution) placed in front. The two cameras were synchronized using a trigger system. Fig. 4 shows 2 samples of images that were captured simultaneously by both cameras.

Using the high resolution infrared and visual images the IR/DIA/PIV processing technique obtains temperature distributions, solids volume fractions and velocities. This process involves image filtration, normalization, interrogation, cross correlation etc. using the method discussed in Patil et al. [20]. The resulting coarse grid data of size (35 × 68) was used for evaluating time-averaged particle volume fractions, fluxes and temperature distributions.
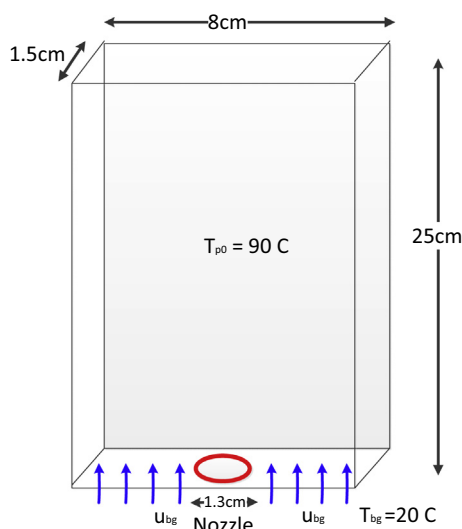

Fig. 3. Experimental set up showing the dimensions of the fluidized bed. This set up had a circular nozzle at the bottom centre of the perforated inlet which has been shown by red circle. (For interpretation of the references to colour in this figure legend, the reader is referred to the web version of this article.)
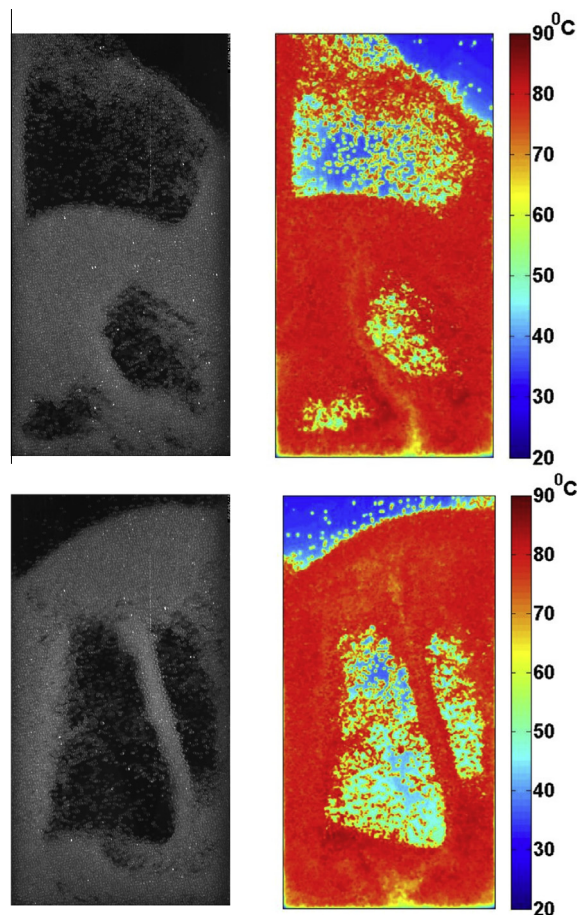

Fig. 4. Instantaneous synchronized visual and infrared images of the pseudo 2-D fluidized bed. These images are for a fluidization run of the bed with 1 mm particles and mass 125 g.

The simulation results were visualized using the Paraview software. The temperature fields from the simulations can be directly compared to the measured IR temperature fields. Fig. 5 shows a series of simulation snapshots along with the IR images corresponding to the same instances in time (1 s, 4 s and 12 s). Due to the flow pattern of particles and gas, a narrow cold zone of particles is seen at the centre bottom of the pseudo 2-D fluidized bed in the IR experiments (Figs. 4 and 5). These narrow channels of cold particles swivel around at the base during fluidization. This phenomena is faithfully reproduced in the simulations, see Fig. 5.

In order to compare the experimental profiles of volume fractions and fluxes with the simulation data, the grid size in the simulations was chosen to correspond with the experimental coarse 'interrogation-window' grid (i.e. 35 × 68). The data processing for both the experiments and simulations was performed using Matlab scripts where the solids volume fraction, velocity and temporal distribution were obtained on the interrogation-window grid. For the experimental data the DIA procedure as described in [20] was used to obtain volume fractions. These instantaneous solids volume fraction fields are coupled with PIV data and/or temperature fields form the IR camera to obtain (time-averaged) fields and fluxes. For the simulations the same processing was used,
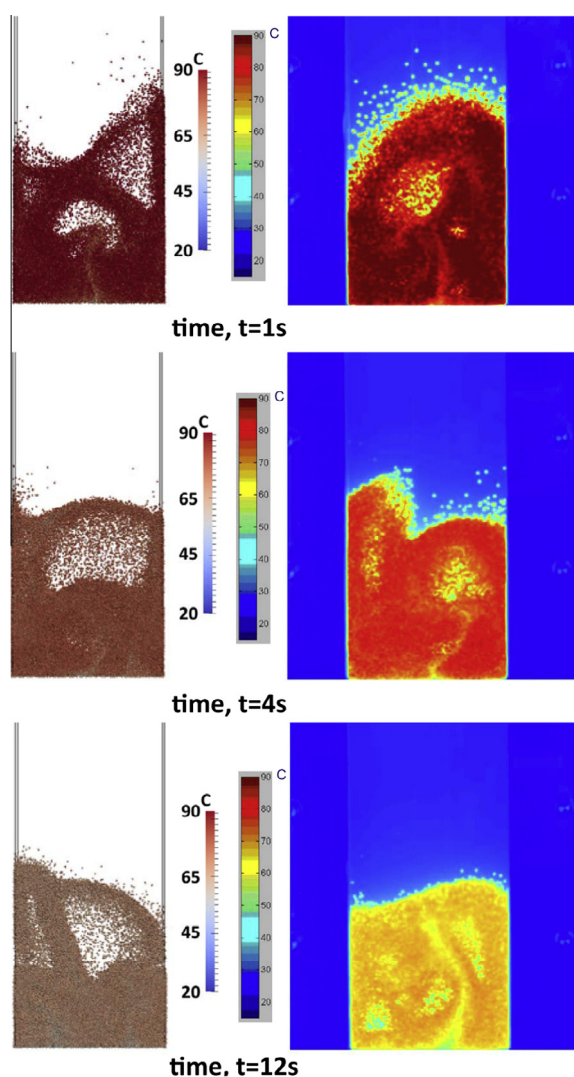
except that in this case some properties like solids volume fractions can be directly extracted from the data. The comparison of the resulting processed images will be shown in the next section.

4. Results and discussion

4.1. Matching cooling curves

The CFD–DEM simulation results were obtained with a code that implemented the heat transfer mechanisms discussed in Section 2. As stated in that section, the gas–wall heat transfer coefficient, h_w, was used as an adjustable parameter. This was achieved by using a range of reasonable wall heat transfer coefficient values.

Starting from an adiabatic wall the wall heat loss coefficient was increased (0, 50, 100, 250, 350 W/m² K). These varying heat loss coefficients determine the resistance to gas–wall heat transfer near the wall. From the thermal conductivity $k_g = 0.025$ W/m K the thickness of the thermal resistance layer can be estimated, using Eq. (17), and has been tabulated here in Table 3.

It is observed that the temperature decline is faster with increasing wall heat loss coefficient. This can be seen in Fig. 6. When closely observed, the cooling-rate change is sharper for low heat transfer coefficients (e.g. 0–50 W/m² K). For larger heat transfer coefficients a further increase does not significantly affect the cooling rate anymore (e.g. 250–350 W/m² K). This limiting behaviour indicates that the heat transfer from the hot gas in the fluidized bed to the environment reaches a saturation. In this case the resistance of the gas–wall heat-transfer mechanism is negligible compared to other resistances.

When these curves are compared to fluidization experiments with fluidization velocity 1.2 m/s as shown in Fig. 6a the temperature decay is slightly faster in experiments than in the simulations (at saturated h_w). However, for the case of fluidization velocity 1.54 m/s it is observed that the experiments and simulations match well for $h_w = 350$ W/m² K, see Fig. 6b. Similarly, for a higher fluidization velocity of 1.71 m/s also the experiments matched well with simulations at this saturated value of h_w. Fig. 7 shows mean particle temperature profiles for experiments and CFD–DEM simulations at $h_w = 350$ W/m² K for fluidization velocities: 1.2, 1.54 and 1.71 m/s (particle size 1 mm and bed mass 75 g). CFD–DEM simulations that were done for bed mass size of 125 g and particle size 1 mm also match reasonably well with experiments. Here, once again, the saturation in mean particle temperature profile slope was reached at $h_w = 350$ W/m² K. Fig. 8 shows these profiles for fluidization velocities 1.2 m/s and 1.54 m/s.

In the combined DIA/PIV/IR measuring system that was developed [20], experiments were also conducted on Geldart B 0.5 mm particles. Comparisons for these particle sizes have not been included in this paper because the simulated cooling profile slopes were much smaller compared to experiments. This is an indication that for 0.5 mm particles there are certain mechanisms of heat loss to the wall that are not getting accounted for in the CFD–DEM. We speculate that the mechanisms discussed in Section 2.5 play an important role in reality while they are not incorporated in the model. As discussed earlier these mechanisms due to longer


Fig. 5. Instantaneous simulation images visualized by Paraview and infrared images recorded by IR camera at various time instants of fluidization. These images are for fluidization run of 1 mm particle bed and bed mass 75 g.

Table 3
Fitted gas–wall heat transfer coefficients and their respective thermal resistance layer thickness.

Heat loss coefficient h_w (W/m² K)	Thickness δ_l (mm)
50	0.5
100	0.25
250	0.01
350	0.007
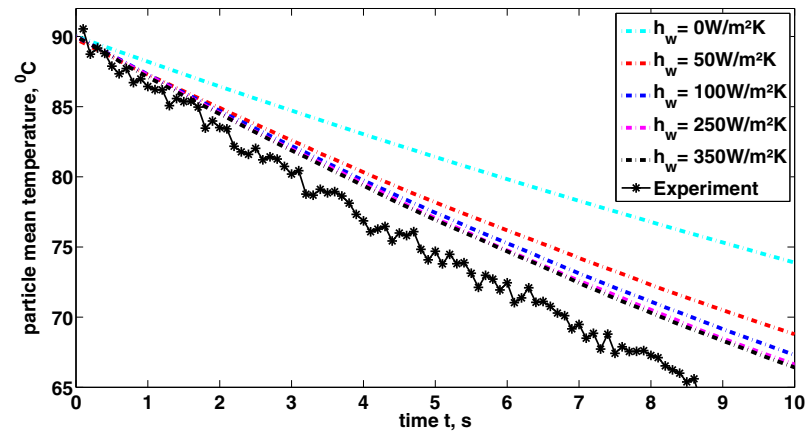
(a) Mean particle temperature profiles with varying wall heat loss coefficient for fluidized bed with 1 mm particles, $u_{\rm bg} = 1.2$ m/s and bed mass 75 g with comparisons to experiments.
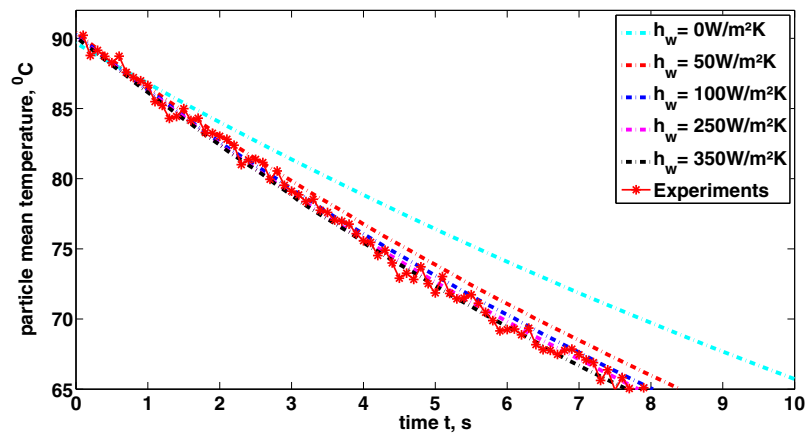
(b) Mean particle temperature profiles with varying wall heat loss coefficient for fluidized bed with 1mm particles, $u_{\rm bg} = 1.54$ m/s and bed mass 75 g with comparisons to experiments.

Fig. 6. Plots showing the effect of varying wall heat loss coefficient on mean particle temperature profiles during CFD–DEM simulations and their comparison with experiments.
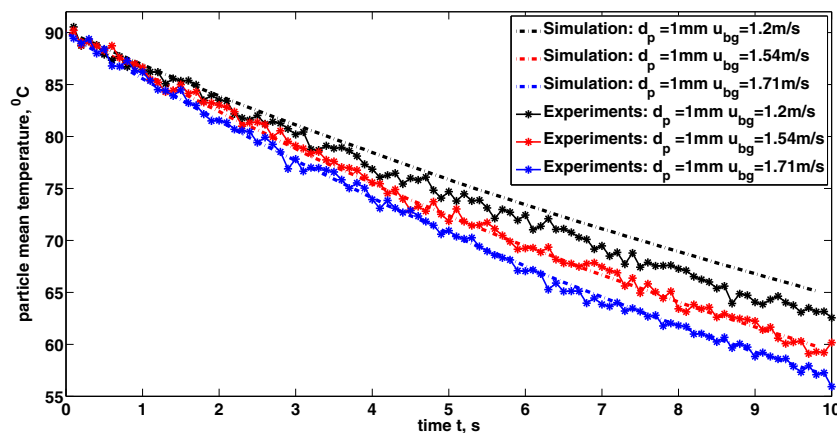

Fig. 7. Comparison between experiments and simulation between cooling profile for fluidized bed with 1 mm particles and bed mass 75 g and $h_w = 350$ W/m^2 K.
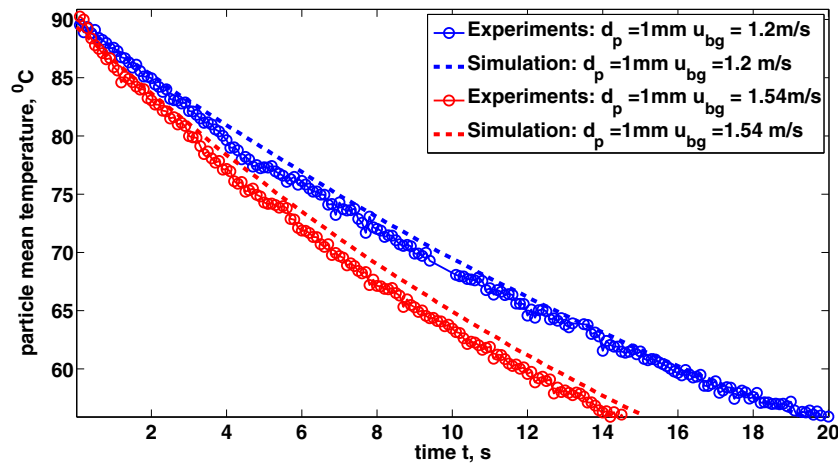
Fig. 8. Comparison between experiments and simulation between cooling profile for fluidized bed with 1 mm particles and bed mass 125 g with the wall heat loss coefficient of 350 W/m² K.

contacts of particles with wall could be a stronger contributor to heat loss for smaller Geldart B type of particles. Unaccounted mechanism like longer contact times due to momentary stagnation of particles must be playing a more dominant role at lower background gas velocities. This is consistent with the deviation found for 1 mm particles at low gas velocity (see Figs. 6a and 7) and for 0.5 mm particles which were fluidized at relatively lower velocities of 0.51 m/s and 0.86 m/s.

4.2. Energy balances

From the CFD–DEM simulations we can obtain information on the relative importance of the several heat-transfer mechanisms at play. From the results shown in Fig. 6a and b the energy loss through the walls could be estimated as the difference in energy lost by the particles in the adiabatic temperature profile and fitted temperature profile. Energy lost by particle collision with the wall was recorded and maintained in the non-adiabatic simulations itself. So, the heat lost through the 3 mechanisms in the CFD–DEM simulations could be obtained and have been summarized hereby in Table 4. The fitted gas–wall heat transfer coefficient used for these simulations is the saturated value, i.e., 350 W/m² K.

From the results in Table 4 it is seen that heat loss through the exit has the highest contribution to the heat loss followed by gas-to-wall heat transfer. Heat transfer due to particle collisions with the wall is very small or negligible. It is further observed that with increasing background gas velocity the heat loss through all of the mechanisms increased. This is expected as an increase in the velocity of background gas increases the gas flow and gas particle heat interaction thus increasing the heat moving out of the outlet. The higher background velocity also means that the particles are more vigorously fluidized leading to a enhanced mixing in the bed. This decreases δ_l the thickness of the film layer of heat resistance near the wall causing a higher wall heat loss as well. This

same phenomena is also responsible for the increase in particle–wall collision heat loss as vigorous fluidization increase collision rates. It can also be observed that with increase in bed mass the heat transfer by all of the mechanisms increases.

4.3. Instantaneous fields and distributions

In this section the instantaneous experimental images obtained with the DIA/IR technique and simulation data are compared. The DIA images of instantaneous solids volume fields are shown in Fig. 9a and simulation results in Fig. 9b. Similarly, both measured and computed temperature fields are depicted in Fig. 9c and d, respectively.

From the instantaneous 2-D field measurements and simulations particle temperature distributions over the bed were obtained. These temperature distributions have been plotted, at 4 different times, namely: 1 s, 5 s, 10 s and 13 s, in Fig. 9e and f. From these distributions it is clear that the simulations produce sharper profiles than the experiments. This could be due to unaccounted forms of heat transfer mechanisms that was discussed earlier in Section 2.5. However, in the next subsections some other analysis on time-averaged spatial distribution inconsistencies will be presented. There some limitations in the current IR technique will be discussed. The less sharp temperature distribution for experiments could at least be partly attributed to these measurement issues.

In Patil et al. [20] it was shown that the standard deviation of the particle temperature distribution profile decreased with decreasing temperature of the particles. This was due to the reducing driving force which is the temperature difference between inlet gas and fluidizing particles. This can also be seen here in the experimental and simulation results of Fig. 9e and f. The spread of the temperature distribution decreases as the temperature of particles decreases for both experiments and simulations reaffirming the trend of decreasing standard deviation as the bed cools.

Table 4
Energy analysis from simulation data.

Particle size d_p, mm	u_{bg}, m/s	Bed mass, g	Heat lost through outlet, W	Heat lost by gas to wall contact, W	Heat lost by particle–wall collision, W
1	1.2	75	101.750	46.648	0.286
1	1.54	75	153.091	49.427	0.343
1	1.71	75	175.77	59.250	0.348
1	1.2	125	138.048	82.024	0.716
1	1.54	125	171.234	103.638	0.732

(a) ε_p-exp.   (b) ε_p-sim.   (c) T-exp.   (d) T-sim.

(e) Experimentally determined temperature distribution

(f) Temperature distribution from simulations
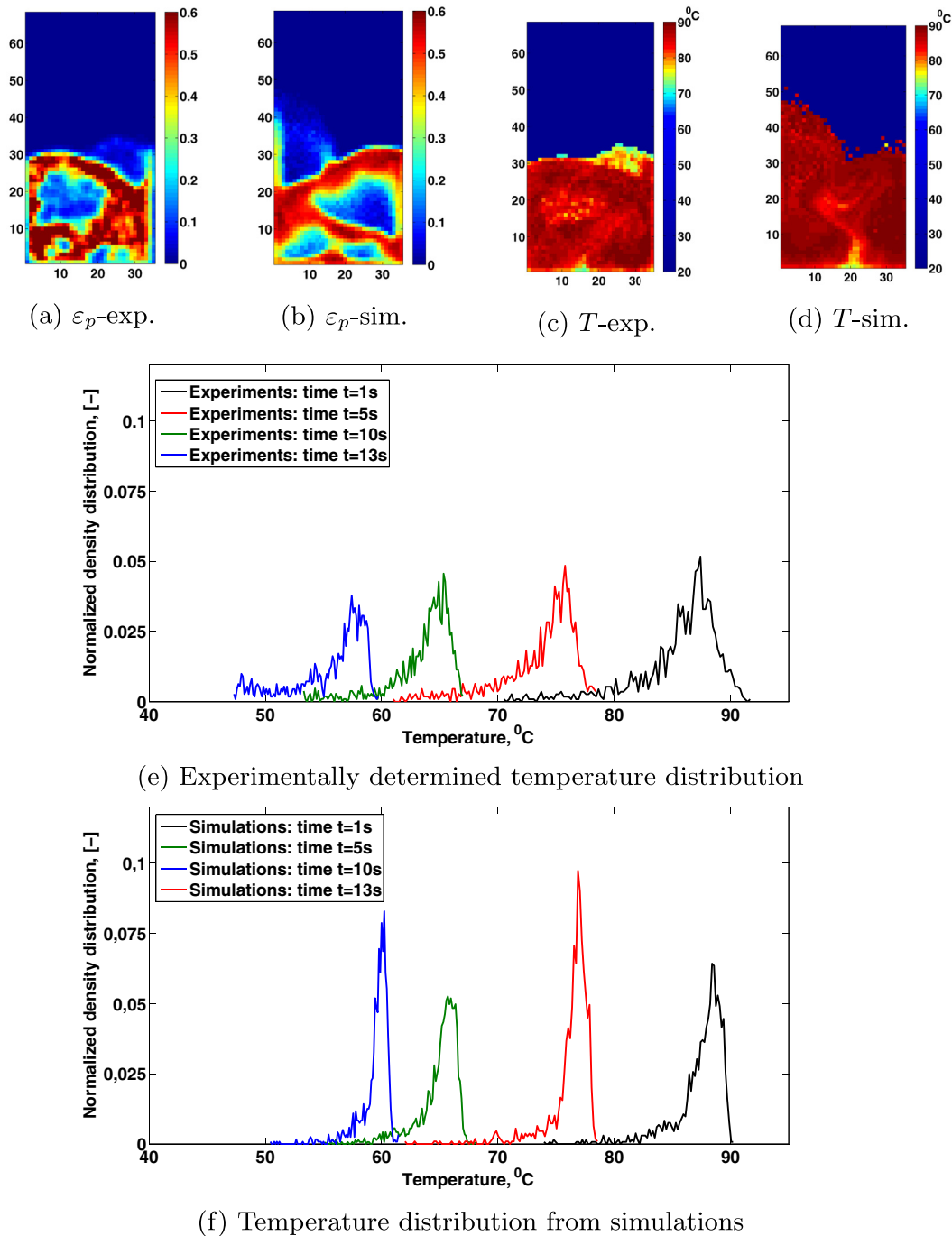
Fig. 9. The depicted data is for a fluidization run at $u_{\mathrm{bg}} = 1.2$ m/s, bed mass 75 g and $d_p = 1$ mm. The first row shows comparisons of instantaneous solids volume fraction and temperature fields as measured and simulated. (e) and (f) shows instantaneous temperature distributions obtained from interrogation grid sized data of experiments and simulations respectively. The black distribution curves in both these plots correspond to the fields shown in (c) and (d).

4.4. Time-averaged spatial data

The newly developed IR/DIA/PIV experimental technique facilitates the comparison between spatial distributions from experiments and simulation. Using this non-invasive visual and infrared measurements detailed information on solids volume fraction fields, volume fluxes vector plots and temperature fields were obtained. These fields were compared with the simulation results. The solid volume fraction field and volume flux vector plots are based on previous work by de Jong et al. [18].

With the incorporation of infrared the temperature distribution profiles have been added. The presented time-averaged 'temperature fields' are actually the relative deviation from the spatially-averaged mean temperature, $\langle T_p \rangle_\varepsilon$. Since the driving force of the heat transfer changes as the particles get colder the deviation of the temperature from the mean is non-dimensionalized by dividing it by the temperature difference between mean particle temperature and inlet gas temperature,

$$\overline{\Gamma_p}(i,j) = \frac{1}{\sum_t \varepsilon_p(t,i,j)} \sum_t \varepsilon_p(t,i,j) \frac{T_p(t,i,j) - \langle T_p(t) \rangle_\varepsilon}{\langle T_p(t) \rangle_\varepsilon - T_{g,\mathrm{in}}(t)}. \qquad (21)$$

The reason for defining this quantity is the fact that when the bed is as at the inlet-gas temperature there will be no inhomogeneities in

the particle temperatures. When the bed is cooling it is expected that the variation of particle temperatures in the bed will be proportional to the thermal driving force, $\langle T_p(t) \rangle_\varepsilon - T_{g,in}$. Therefore this non-dimensional temperature is expected to be a time independent good approximation and time-averaging of this quantity makes sense. A more in-depth discussion of this quantity is provided in [20].

Here we focus on time-averaged results for the bed filled with 1 mm particles and bed masses 75 g and 125 g. Figs. 10 and 11 show time-averaged fields for fluidization velocities 1.2 m/s and 1.71 m/s, respectively, and bed mass 75 g. Fig. 12 shows the fields for $u_{bg} = 1.54$ m/s and bed mass 125 g. All 3 figures each compare three properties, namely, time-averaged: solids volume fractions, mass fluxes and particle-temperatures differences with respect to the spatial mean.

It can be seen that the solids volume fraction fields and solids volume flux vector-fields match well for experiments and simulations (see Fig. 10a and b) and (see Fig. 10c and d, respectively). The solids volume fluxes of particles that were experimentally
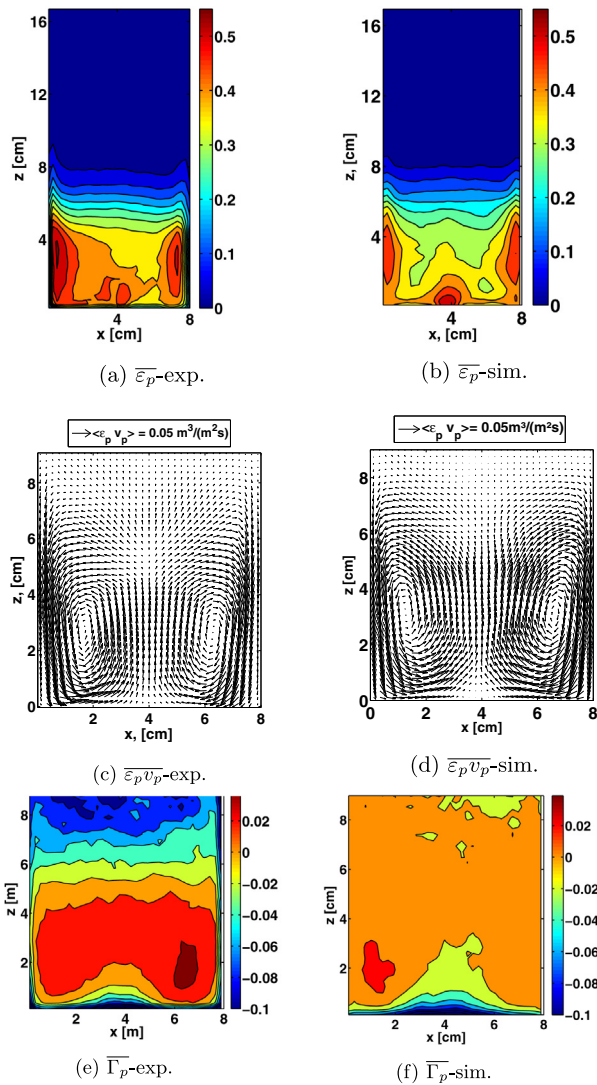

(a) $\overline{\varepsilon_p}$-exp. (b) $\overline{\varepsilon_p}$-sim.

(c) $\overline{\varepsilon_p v_p}$-exp. (d) $\overline{\varepsilon_p v_p}$-sim.

(e) $\overline{\Gamma_p}$-exp. (f) $\overline{\Gamma}$-sim.

Fig. 11. Time-averaged fields for particle size $d_p = 1$ mm and bed mass 75 g. The background velocity $u_{bg} = 1.71$ m/s. The first row of plots, a and b, shows the solids volume fraction in the bed obtained from DIA and simulations, respectively. The second row shows solids volume flux fields obtained by DIA/PIV coupling. The third row shows the time-averaged dimensionless particle temperature, Eq.(21), obtained by DIA/IR coupling.
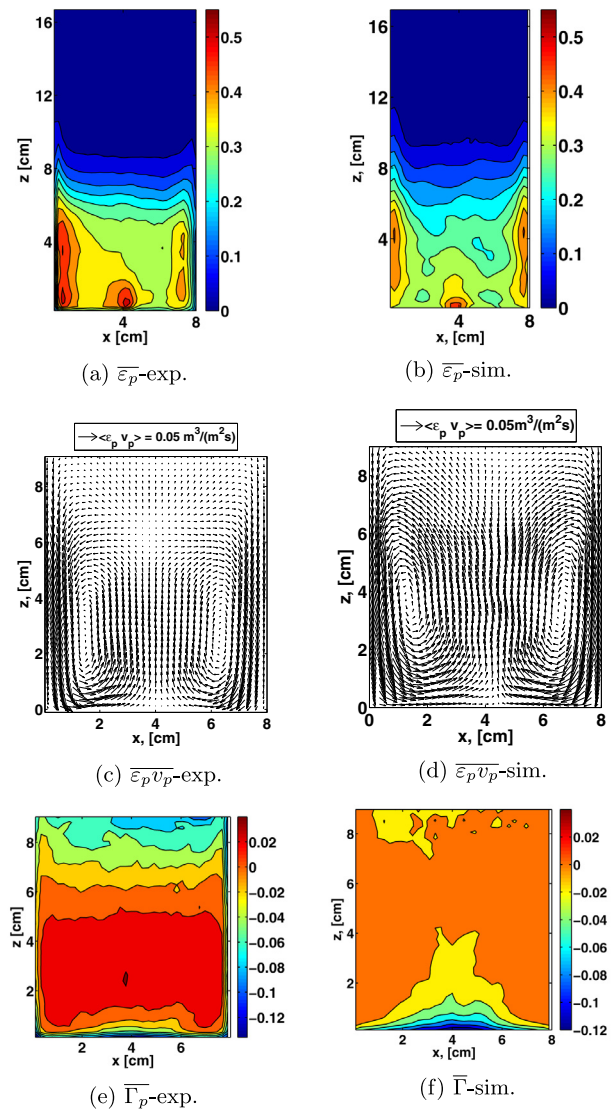
recorded by DIA/PIV and computed by simulations were compared at a height of 2.3 cm above the bottom of the bed in Fig. 14a and b for fluidization velocities 1.2 m/s and 1.71 m/s. This quantitative comparison of the z-component of the solids-volume fluxes is very good. In both cases there is a slight asymmetry. This can be explained by the finite time interval used to perform the averaging. In Fig. 14a the experimental asymmetry seems bigger than the simulated one. Note, however, that at lower gas velocity non-homogeneities due to the distributer plate are more significant in experiments. The most notable difference between the experimental and simulation profiles is the behavior very near the walls. With respect to temperature fields there are some noticeable differences between experiments and simulations in Fig. 10e and f.

The spatial variation of the time-averaged Γ_p lies in the range of -0.1 to 0.04, for example, see Fig. 10e. For example, if the inlet temperature is 20 °C and mean particle temperature is 80 °C) the spread of the particle temperature distribution is in the range of 74–82.4 °C. This magnitude of variations is also clear from Fig. 9e.
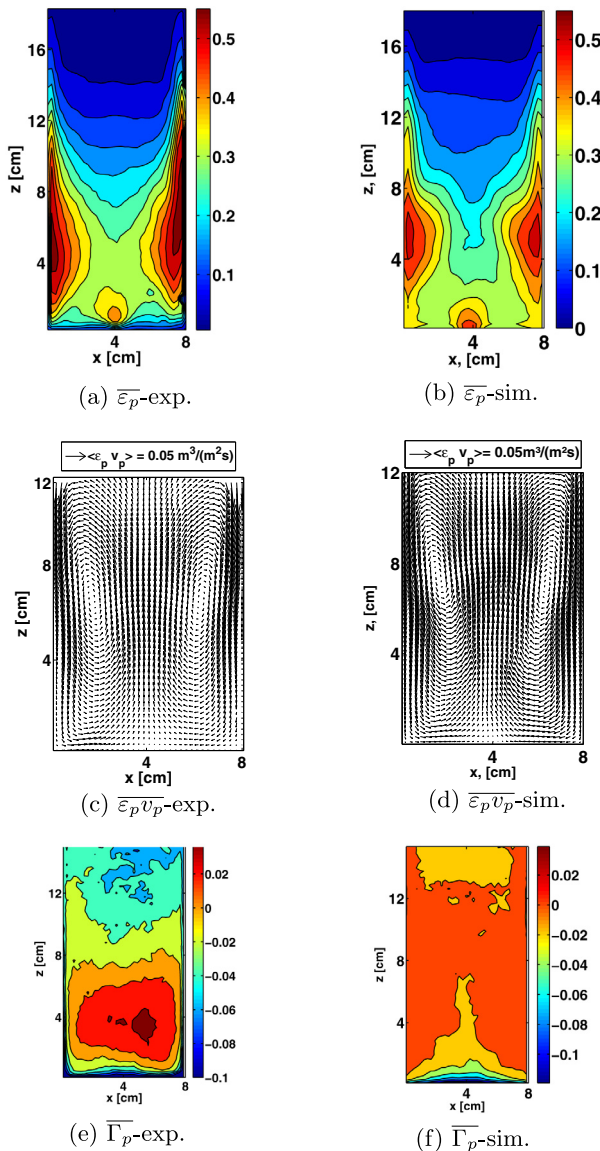

(a) $\overline{\varepsilon_p}$-exp. (b) $\overline{\varepsilon_p}$-sim.

(c) $\overline{\varepsilon_p v_p}$-exp. (d) $\overline{\varepsilon_p v_p}$-sim.

(e) $\overline{\Gamma_p}$-exp. (f) $\overline{\Gamma_p}$-sim.

Fig. 10. Time-averaged fields for particle size $d_p = 1$ mm and bed mass 75 g. The background velocity $u_{bg} = 1.2$ m/s. The first row of plots, a and b, shows the solids volume fraction in the bed obtained from DIA and simulations, respectively. The second row shows solids volume flux fields obtained by DIA/PIV coupling. The third row shows the time-averaged dimensionless particle temperature, Eq. (21), obtained by DIA/IR coupling.

(a) $\overline{\varepsilon_p}$-exp.

(b) $\overline{\varepsilon_p}$-sim.

(c) $\overline{\varepsilon_p v_p}$-exp.

(d) $\overline{\varepsilon_p v_p}$-sim.

(e) $\overline{\Gamma_p}$-exp.

(f) $\overline{\Gamma_p}$-sim.

Fig. 12. Time-averaged fields for particle size $d_p = 1$ mm and bed mass 125 g. The background velocity $u_{bg} = 1.54$ m/s. The first row of plots, a and b, shows the solids volume fraction in the bed obtained from DIA and simulations respectively. The second row shows solids volume flux fields obtained by DIA/PIV coupling. The third row shows the time-averaged dimensionless particle temperature, Eq.(21), obtained by DIA/IR coupling.

The cold inlet gas enters from the bottom in Fig. 10e and f where it can be seen that at the bottom the non-dimensionalized temperature deviation $\overline{\Gamma_p}$ is close to -0.1. Due to the high back mixing rate in fluidized beds this deviation sharply rises from -0.1 as we move upwards in the bed. In the centre of the bed the temperature is close to or slightly higher than the mean. In experiments it reaches close to 0.02 and in simulation it is closer to 0.00 as shown in Fig. 10e and f. In both cases at the centre bottom a narrow rise of cold zone (-0.1 to 0.0) can be observed. This follows from the flow pattern of the particles which can be observed from the solids volume flux distributions shown in Fig. 10c and d.

However, in the upper part of the bed there are some striking differences between experiments and simulations. Starting from the upper centre of the bed $\overline{\Gamma_p}$ declines in the upward direction from 0 going towards -0.1 for experiments. But in the simulations

case the temperature deviation remains uniform slightly above the mean throughout this region also. There is an observed decline at a much higher height than in the experiments. This can be observed in the simulation distribution plots of Fig. 11f (height 7–8 cm) and Fig. 12f (height 12 cm).

Γ_p represents the temperature deviation from the mean. In the experimental distribution, Γ_p in the upper half of the bed is lower than in the simulation. This causes the Γ_p in the central part of the bed deviate more toward the higher side in experiments, because the mean of the deviation should equal zero. The deviation in lower half of the bed is less significant because the bed is denser here compared to the upper half and therefore gets more statistical weight (see Eq. (21)).

The upper region of the bed is a sparse region where the bed density is low. It has been shown previously in Patil et al. [20] that the IR measuring system measures a temperature of about 1 °C lower when the particles are in a low density region of the bed. This is one of the reasons contributing to the differences. However, the magnitude of this error in the IR-measurement is not high enough to explain the full mismatch with the simulation result. Another factor that might contribute to the deviation is the higher velocities of particles in the upper half of the bed, i.e., the free board region. The IR integration time for the IR camera was set at 600 µs in the experiments Patil et al. [20]. If particles travel at high enough velocities to translate one pixel or more during this integration time then its image will be blurred. This means that the image of the particle will be smeared out over more pixels with a lower intensity per pixel. This lower intensity is next interpreted as a lower temperature. Thus we expect that in the lower half of the bed the measurement is most accurate and this accuracy reduces as we move upward in the bed. Since these distributions represented by Γ_p are somewhat abstract it becomes difficult to imagine the differences between experiments and simulations in the upper half of the bed in terms of absolute temperatures. In order to be able to do this we show a representative profile in an alternative way. Assuming the mean temperature of the bed was constant at 70 °C the actual temperature distribution can be calculated back from the Γ_p distribution. This reconstructed temperature distribution for a 75 g bed and background gas velocity 1.2 m/s is given by in Fig. 13.

4.5. Instantaneous temperature profiles

At the centre bottom of the pseudo 2-D bed the temperature varies most rapidly. Therefore we will have a closer look at this region. In Fig. 15 the change in temperature along the centre axis of the bed is shown for different times ($d_p = 1$ mm and 75 g bed mass). Note that here, differently from Patil et al. [20], the axial temperature profiles are considered at the coarse interrogation grid to be able to compare experiments and simulations. It is to be noted that these profiles are obtained by averaging the axial temperature profiles over every 20 images. Since images were recorded at the rate of 0.1 s per image the mean temperature thus obtained was representative of 1 s, 3 s, 5 s,….

In Fig. 15 it is observed that in experiments the particles start out with a lower temperature near the bottom than in the simulations. Moreover, the temperature gradient close to the bottom is larger for experiments than simulations. When calculated with the data available in this figure, for experiments this gradient varied between 2.4 °C/mm and 1.53 °C/mm and for simulations it was between 1.01 °C/mm and 0.43 °C/mm. We think that the unaccounted heat-transfer mechanisms, discussed in Section 2.5, causes this lower gradient in simulations compared to experiments.
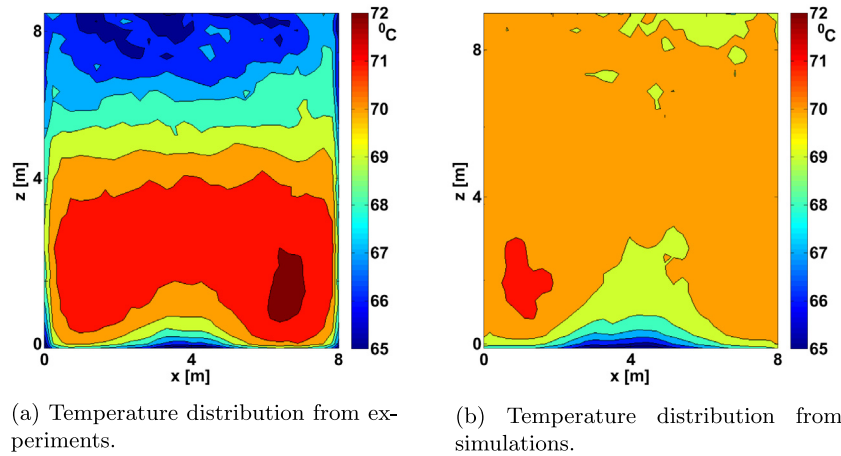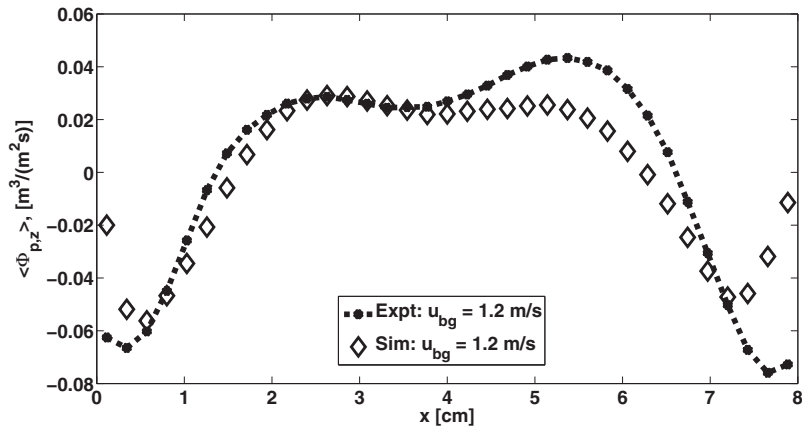
(a) Temperature distribution from experiments.

(b) Temperature distribution from simulations.

Fig. 13. Reconstructed time-averaged temperature distribution for particle size $d_p = 1$ mm, bed mass 75 g and background velocity $u_{bg} = 1.2$ m/s under the assumption that the mean temperature of the particles is constant at 70 °C.

(a) The axial component of the solids volume flux at height 2.3 mm above the bottom of the fluidized bed for 1 mm particle size and fluidization velocity $u_{bg} = 1.2$ m/s.
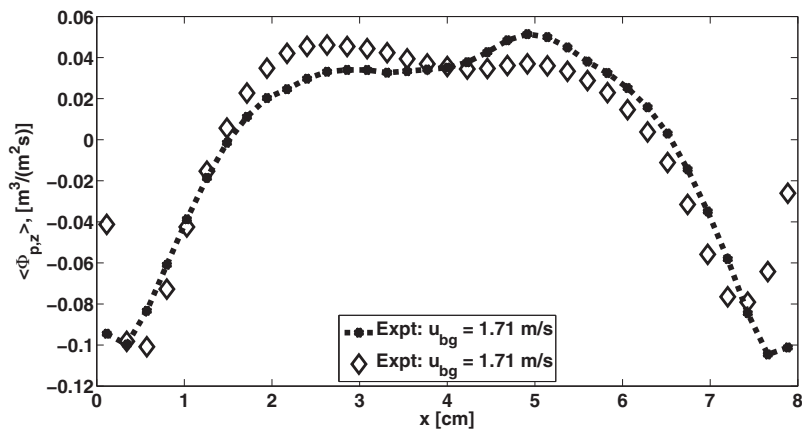
(b) The axial component of the solids volume flux at height 2.3 mm above the bottom of the fluidized bed for 1 mm particle size and fluidization velocity $u_{bg} = 1.71$ m/s.

Fig. 14. The axial component of the solids volume flux at height 2.3 mm above the bottom of the fluidized bed for 1 mm particle size.
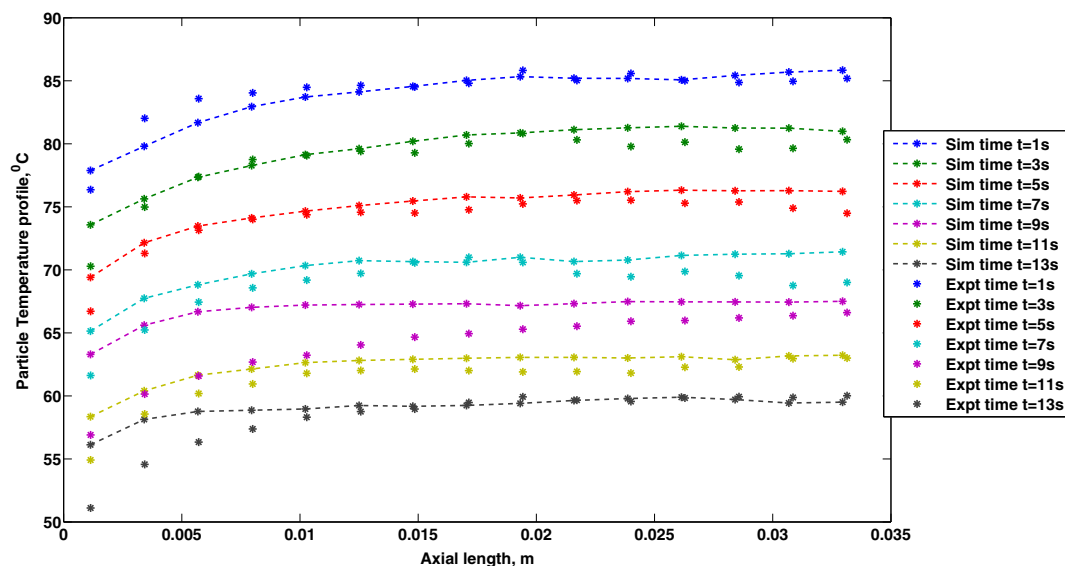
Fig. 15. Axial line temperature profile (from the centre) comparison between experiments and simulation between cooling profile for fluidized bed with 1 mm particles and bed mass 75 g.

5. Conclusion

This work introduces a CFD–DEM modeling of a gas–solid fluidized bed which incorporates various mechanisms of heat transfer. These mechanisms include gas-particle, particle–particle, gas–wall and particle wall heat transfer. The unknown fitted gas–wall heat transfer coefficient was used to match experiments and simulations results with respect to the cooling curves of the beds.

A detailed comparison of experimental and simulation data has been made and analyzed for Geldart D type 1 mm particles. Solids volume fractions and solids volume fluxes both compared well. For the temperature fields the comparison was favorable in the lower half of the bed but less favorable in the upper part. This mismatch is well explained by experimental deviations: namely the dependence of IR results on local solids volume fraction (lower in the top part) and particle velocities (higher in the top part). For highly accurate temperature measurements using IR thermography it therefore might be needed to use calibrations that take into account the local solids volume fractions and local particulate velocities. Note that this would give a further integration of the DIA and IR methods. Furthermore the axial temperature profiles in z direction are sharper for experiments compared to the simulations. The reason for this difference can be mainly attributed to mechanisms of unaccounted forms of heat transfer.

The comparison of CFD–DEM simulations and IR/PIV/DIA has provided much insight in both the modeling and the simulations. It indicates several ways to improve both the modeling and the experiments. For the state-of-the-art CFD–DEM the hydrodynamics is modeled accurately. The heat-transfer is semi-quantitatively correct. The results suggest that in the modeling an extra heat-transfer mechanism should be included, probably due to conduction by the solids phase. It will be challenging to incorporate this in the CFD–DEM methodology which was not attempted in the current paper.

Acknowledgments

References

[1] N.G. Deen, M. van Sint Annaland, M.A. van der Hoef, J.A.M. Kuipers, Review of discrete particle modeling of fluidized beds, Chem. Eng. Sci. 62 (2007) 28–44.
[2] H.P. Zhu, Z.Y. Zhou, R.Y. Yang, A.B. Yu, Discrete particle simulation of particulate systems: theoretical developments, Chem. Eng. Sci. 62 (2007) 3378–3396.
[3] A.V. Patil, E.A.J.F. Peters, T. Kolkman, J.A.M. Kuipers, Modeling bubble heat transfer in gas–solid fluidized beds using DEM, Chem. Eng. Sci. 105 (2014) 121–131.
[4] J. Sun, M.M. Chen, A theoretical analysis of heat transfer due to particle impact, Int. J. Heat Mass Transfer 31 (1988) 969–975.
[5] D. Zhang, W.J. Whiten, An efficient calculation method for particle motion in discrete element simulation, Powder Technol. 98 (1998) 223–230.
[6] S.-S. Hsiau, Effective thermal conductivities of a single species and a binary mixture of granular materials, Int. J. Multiphase Flow 26 (2000) 83–97.
[7] D. Lathouwers, J. Bellan, Modeling of dense gas–solid reactive mixtures applied to biomass pyrolysis in a fluidized bed, Int. J. Multiphase Flow 27 (2001) 2155–2187.
[8] Z. Mansoori, M. Saffar-Avval, H.B. Tabrizi, B. Dabir, G. Ahmadi, Inter-particle heat transfer in a riser of gas–solid turbulent flows, Powder Technol. 159 (2005) 35–45.
[9] Z. Zhou, P. Zulli, A new computational method for studying heat transfer in fluid bed reactors, Powder Technol. 197 (2009) 102–110.
[10] Y. Kaneko, T. Shiojima, M. Horio, DEM simulation of fluidized beds for gas-phase olefin polymerization, Chem. Eng. Sci. 54 (1999) 5809–5821.
[11] Z. Zhou, A. Yu, P. Zulli, A new computational method for studying heat transfer in fluid bed reactors, Powder Technol. 197 (2010) 102–110.
[12] J. Saayman, W. Nicol, J.R. van Ommen, R.F. Mudde, Fast X-ray tomography for the quantification of the bubbling, turbulent and fast fluidization flow regimes and void structures, Chem. Eng. J. 234 (2013) 437–447.
[13] J.A. Laverman, I. Roghair, M. van sint Annaland, J.A.M. Kuipers, Investigation into the hydrodynamics of gas–solid fluidized beds using particle image velocimetry coupled with digital image analysis, Can. J. Chem. Eng. 86 (2008) 523–535.
[14] S. Liu, Q. Chen, H.G. Wang, F. Jiang, I. Ismail, W. Yang, Electrical capacitance tomography for gas–solids flow measurement for circulating fluidized beds, Flow Measur. Instrument. 16 (2005) 135–144. Tomographic Techniques for Multiphase Flow Measurements 4th International Symposium on Measurement Techniques for Multiphase Flows.
[15] J. Laverman, X. Fan, A. Ingram, M. van Sint Annaland, D. Parker, J.P.K. Seville, J.A.M. Kuipers, Experimental study on the influence of bed material on the scaling of solids circulation patterns in 3d bubbling gas–solid fluidized beds of glass and polyethylene using positron emission particle tracking, Powder Technol. 224 (2012) 297–305.
[16] K.A. Buist, A.C. van der Gaag, N.G. Deen, J.A.M. Kuipers, Improved magnetic particle tracking technique in dense gas fluidized beds, AIChE J. 60 (2014) 3133–3142.
[17] M.S. van Buijtenen, M. Börner, N.G. Deen, S. Heinrich, S. Antonyuk, J.A.M. Kuipers, An experimental study of the effect of collision properties on spout fluidized bed dynamics, Powder Technol. 206 (2011) 139–148.
[18] J.F. de Jong, S.O. Odu, M.S. van Buijtenen, N.G. Deen, M. van Sint Annaland, J.A.M. Kuipers, Development and validation of a novel digital image analysis

method for fluidized bed particle image velocimetry, Powder Technol. 230 (2012) 193–202.

[19] H. Kaplan, Practical applications of infrared thermal sensing and imaging equipment, Tutorial Text Series, Society of Photo Optical, 2007.

[20] A.V. Patil, E.A.J.F. Peters, V.S. Sutkar, N.G. Deen, J.A.M. Kuipers, A study of heat transfer in fluidized beds using an integrated DIA/PIV/IR technique, Chem. Eng. J. 259 (2015) 90–106.

[21] R. Beetstra, M.A. van der Hoef, J.A.M. Kuipers, Drag force of intermediate Reynolds number flow past mono- and bidisperse arrays of spheres, AIChE J. 53 (2007) 489–501.

[22] M. Syamlal, D. Gidaspow, Hydrodynamics of fluidization: prediction of wall to bed heat transfer coefficients, AIChE J. 31 (1985) 127–135.

[23] D.J. Gunn, Transfer of heat or mass to particles in fixed and fluidised beds, Int. J. Heat Mass Transfer 21 (1978) 467–476.

[24] Q.F. Hou, Z.Y. Zhou, A.B. Yu, Computational study of heat transfer in a bubbling fluidized bed with a horizontal tube, AIChE J. 58 (2012) 1422–1434.

[25] P.A. Cundall, O.D.L. Strack, A discrete numerical model for granular assemblies, Geotechnique 29 (1979) 47–65.

[26] D. Kunii, O. Levenspiel, Fluidization engineering, Butterworth–Heinemann Series in Chemical Engineering, Butterworth–Heinemann Limited, 1991.